Title

High-Energy Aqueous Sodium-Ion Batteries Using Water-in-Salt Electrolytes and 3D Structured Electrodes.

Journal

ACS Applied Materials & Interfaces, 17(5)

Authors

Yang, Zhiyin
Huang, Ailun
Lin, Cheng-Wei
et al.

Publication Date

2025-02-05

DOI

10.1021/acsami.4c15832

Peer reviewed

ACS APPLIED MATERIALS & INTERFACES

www.acsami.org

Research Article

High-Energy Aqueous Sodium-Ion Batteries Using Water-in-Salt Electrolytes and 3D Structured Electrodes

Zhiyin Yang, Ailun Huang, Cheng-Wei Lin, Bradley C. Kroes, Xueying Chang, Maher F. El-Kady, Yuzhang Li, and Richard B. Kaner*

Cite This: *ACS Appl. Mater. Interfaces* 2025, 17, 7595−7606

Read Online

ACCESS | Metrics & More | Article Recommendations | Supporting Information

ABSTRACT: Aqueous sodium-ion batteries (SIBs) are gradually being recognized as viable solutions for large-scale energy storage because of their inherent safety as well as low cost. However, despite recent advancements in water-in-salt electrolyte technologies, the challenge of identifying anode materials with sufficient specific capacity persists, complicating the wider adoption of these batteries. This study introduces an innovative and straightforward approach for synthesizing vanadium oxide laser-scribed graphene (VO_x-LSG) composites, which function as effective anode materials in aqueous sodium-ion batteries. By combining a rapid laser-scribing technique with precise thermal control, the method not only allows for changing the morphology of the vanadium oxide, but also tuning its oxidation state. This is achieved while embedding these electrochemically active particles within a highly conductive graphene scaffold. When paired with a Prussian blue-based cathode ($Na_{1.88}Mn[Fe(CN)_6]_{0.97}$) in a concentrated $NaClO_4$-based aqueous electrolyte, the battery's charge storage mechanism is found to be largely surface-controlled, leading to exceptional rate performance. The full cell demonstrates specific capacities of 128 mA h/g@0.05 A/g and 65.6 mA h/g@1 A/g, with an energy density of 47.7 W h/kg, outperforming many existing aqueous sodium-ion batteries. This strategy offers a promising path forward for integrating efficient, eco-friendly, and low-cost anode materials into large energy storage devices and systems.

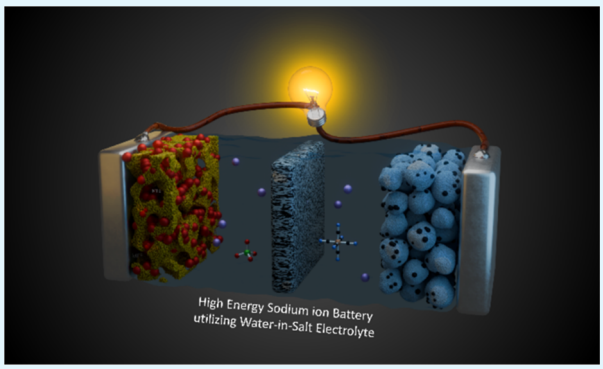

KEYWORDS: *aqueous sodium-ion batteries, laser-scribing, vanadium oxide, water-in-salt electrolyte, graphene*

INTRODUCTION

With accelerating population growth and economic development, there is an increasing global demand for energy, especially from renewable energy sources such as wind and solar power for modern energy grids.[1] Among the many energy storage solutions under exploration, sodium-ion batteries (SIBs) are emerging as a viable alternative to lithium-ion batteries (LIBs), particularly for grid-scale and large-scale energy storage applications. This is largely resulting from the low cost and widespread availability of sodium.[2−7] In particular, aqueous sodium-ion batteries offer promising potential for large-scale energy storage because of their intrinsic safe operation, nontoxicity, and cost-efficiency.[8] However, the performance of aqueous batteries is limited by several key factors associated with the aqueous electrolyte. For instance, the narrow electrochemical window of water (1.23 V due to HER and ORR) constrains the achievable output voltage and energy density of these batteries. Additionally, significant challenges remain in achieving high Coulombic efficiency and cycling stability, as the evolution of hydrogen and oxygen, especially at low charge/discharge rates, can degrade battery performance.[9]

Recent advances have shown that water-in-salt (WiS) electrolytes can extend the electrochemical stability window to approximately 3 V, facilitating high-voltage chemistries such as those involving Li-ions. This improvement has enabled aqueous batteries to achieve higher energy densities and superior cycling stability, primarily because a solid electrolyte interphase (SEI) forms on the anode surface.[10] This breakthrough has also been successfully used in aqueous-based zinc, sodium, and potassium-ion batteries[11−13] as well as supercapacitors.[14]

Nonetheless, there are still many challenges regarding the development of high-performance electrolytes and electrode materials for electrochemical energy storage in aqueous environments. Despite the cost advantages of aqueous sodium-ion batteries, traditional electrode materials, such as polyanionic compounds,[15] layered oxides,[16] and Prussian blue

Received: September 15, 2024
Revised: January 2, 2025
Accepted: January 5, 2025
Published: January 21, 2025

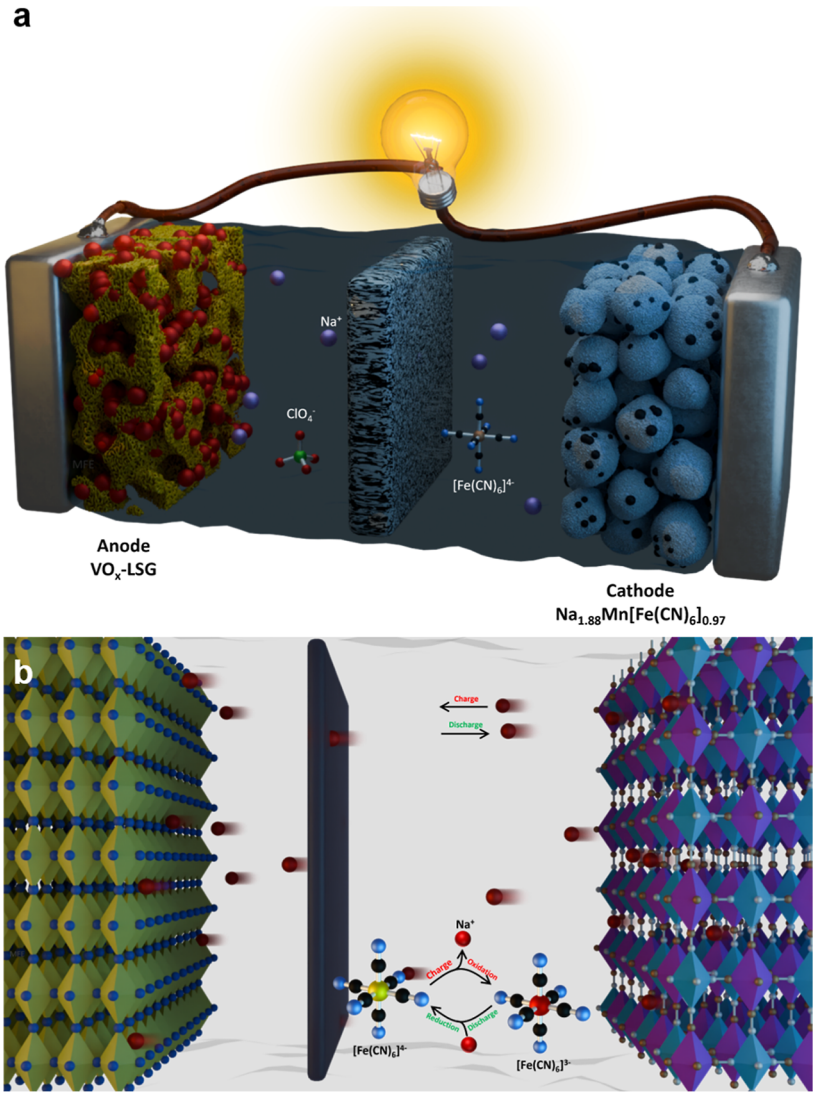

Figure 1. (a) Schematic illustration of the $Na_{1.88}Mn[Fe(CN)_6]_{0.97}$ || VO_x-LSG full cell (b) Charge storage mechanism of the $Na_{1.88}Mn[Fe(CN)_6]_{0.97}$ || VO_x-LSG full cell.

derivatives[17] typically exhibit lower energy densities when compared to those used in lithium-ion systems. A key challenge is the lack of anode materials that can maintain their structural integrity during rapid and repeated insertion/extraction of Na^+ ions. Although $NaTi_2(PO_4)_3$, which possesses a known sodium superionic conductor (NASICON) structure, has shown promise as an anode material because of its 3D open framework and appropriate negative voltage window, its low electronic conductivity—due to the separation of TiO_6 octahedra—presents a significant obstacle to its broader commercial use.[18,19] Vanadium oxides are attractive candidates for anode materials in aqueous sodium-ion batteries because they have many oxidation states (ranging from V^{2+} to V^{5+}), which support diverse redox reactions. The unique layered structure of vanadium oxides enables ultrafast 2D ion diffusion and provides the materials with excellent electrochemical properties.[20,21]

In this paper, we present a straightforward two-step synthesis approach to develop a vanadium oxide laser-scribed graphene (VO_x-LSG) composite material as an anode for aqueous sodium-ion batteries. By using a VCl_3/graphene oxide (GO) solution as the precursor, a composite with nanoscale vanadium (+4/+5) particles uniformly distributed on an expanded 3D graphene network is achieved through laser-scribing and controlled heating. The resulting material exhibits enhanced charge storage capacity due to the uniform anchoring of VO_x nanoparticles on the conductive graphene scaffold. When combined with a Prussian blue cathode ($Na_{1.88}Mn[Fe(CN)_6]_{0.97}$), the full cell exhibits surface-controlled charge storage, enabling excellent rate performance and fast charging capabilities (Figure 1). The full cell achieves fast charging (65.6 mA h/g capacity@1 A/g), high specific capacity (128 mA h/g@0.05 A/g), long cycle life (60% after 1000 cycles@1 A/g) and high energy density (83.2 W h/kg).

RESULTS AND DISCUSSION

The anode material, vanadium oxide laser-scribed graphene (VO_x-LSG) was synthesized with a simple method to integrate a pseudocapacitive material into battery applications. This process employs a two-step approach involving laser scribing followed by heating, resulting in a composite where nanosized vanadium oxide particles are uniformly distributed within a three-dimensional graphene matrix. Initially, a solution of VCl_3 was combined with a graphene oxide (GO) dispersion. A

https://doi.org/10.1021/acsami.4c15832
ACS Appl. Mater. Interfaces 2025, 17, 7595−7606

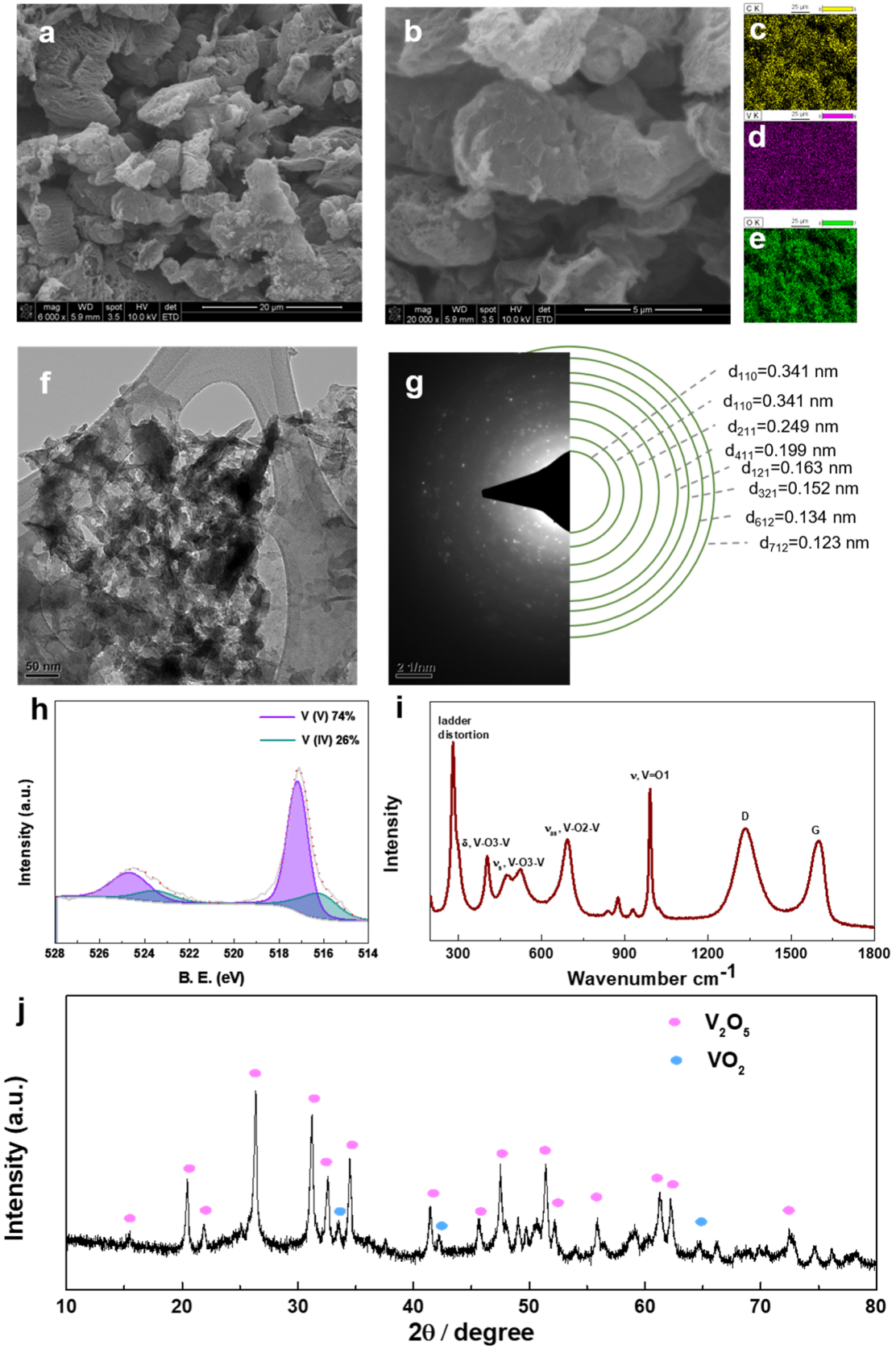

Figure 2. Characterization of the as-synthesized VO_x-LSG composite. (a,b) Low- and high-magnification SEM images of the VO_x-LSG composite. EDS elemental mapping of (c) carbon, (d) oxygen, and (e) vanadium in the VO_x-LSG composite. (f) The bright field TEM images and (g) corresponding SAED patterns of the VO_x-LSG composite. (h) XPS V 2p1/2 and V 2p3/2 spectra of a VO_x-LSG composite. (i) Raman spectra of the composite showing V_2O_5 and graphene features. (j) XRD pattern of VO_x-LSG matching V_2O_5 (JCPDS no. 00−041−1426) and VO_2 (JCPDS no. 00−044−0252).

https://doi.org/10.1021/acsami.4c15832
ACS Appl. Mater. Interfaces 2025, 17, 7595−7606

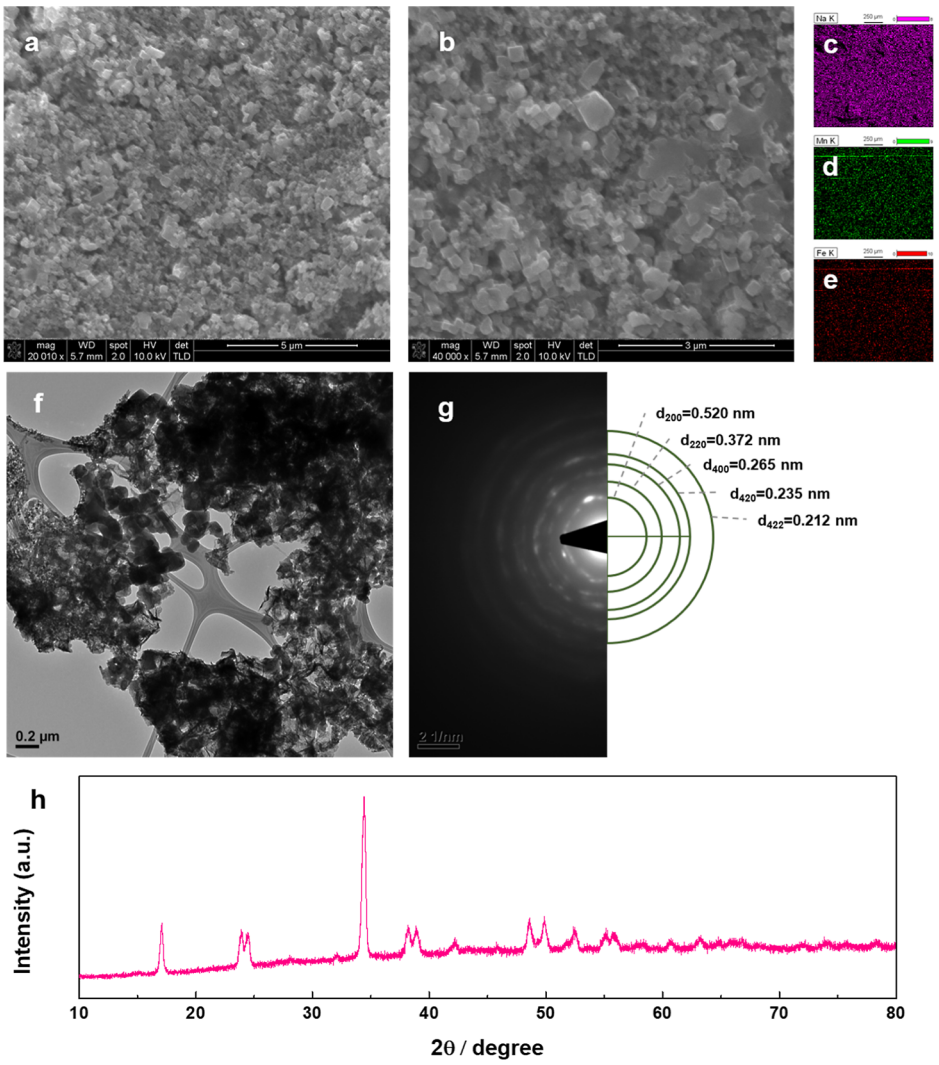

Figure 3. Characterizations of the as-synthesized NaMnHCF composite. (a,b) Low- and high-magnification SEM images of the NaMnHCF composite. EDS elemental mapping of (c) sodium, (d) manganese, and (e) iron in NaMnHCF composite. (f) The bright field TEM image and the (g) corresponding SAED pattern of the NaMnHCF composite. (h) X-ray diffraction (XRD) pattern for the NaMnHCF sample.

syringe pump was used to drop-cast the VCl_3 solution into a GO solution to make sure the VCl_3 solution was uniformly mixed with the GO solution. V^{3+} are thought to function as spacers, preventing the aggregation of GO sheets. Following this, the mixture underwent laser scribing and was subsequently heated to 300 °C for an hour. Previous work has shown that laser scribing transforms the VCl_3-GO film into a range of vanadium oxide species, including VO, V_2O_3, VO_2, and V_2O_5, alongside an expanded graphene network due to the rapid gas release during GO reduction.[22,23] While laser-scribing alone is capable of producing thin-film electrodes suited for supercapacitors reliant on surface charge storage, these electrode materials typically only achieve low areal mass loadings.[24,25] These materials are not ideal for battery-based electrochemistry, because batteries require more uniform electrodes to facilitate ion transport deeper beneath the surface. After the brief heat exposure from the CO_2 laser, VO_x/laser-scribed graphene composite underwent an extended thermal treatment in air, which oxidized the lower-valent VO_x into a layered V_2O_5 structure, enabling two-dimensional diffusion.[26] Upon heating at 300 °C for an hour, the transformation of the VCl_3/GO film into a VO_x-LSG film was completed. Since the heating temperature (300 °C) is below the decomposition threshold of laser-scribed graphene (>400 °C), the graphene remained stable, preventing its oxidation into CO or CO_2. Figure S1 shows the thermogravimetric analysis (TGA) of the VO_x-LSG film that revealed a significant mass loss at 400 °C, indicating approximately 23% of the film is composed of laser-scribed graphene.

SEM images of the VO_x-LSG film are depicted in Figure 2a,b. Figure 2a illustrates the structure and morphology of the laser-scribed graphene, revealing flakes and wrinkles that confirm the effective reduction of graphene oxide (GO) through the laser scribing process. At higher magnification, Figure 2b shows that the VO_x particles are evenly dispersed throughout the three-dimensional graphene scaffold. Energy dispersive spectroscopy (EDS) mapping, shown in Figure 2c–e, confirms the uniform distribution of carbon (C), vanadium (V), and oxygen (O) elements within the VO_x-LSG film. The TEM image in Figure 2f reveals that nanoparticles approximately 40–50 nm in size are evenly distributed on the graphene sheets. SAED pattern in Figure 2g indicates the presence of orthorhombic V_2O_5 structure (JCPDS no. 00–041–1426), with clear diffraction spots corresponding to the

https://doi.org/10.1021/acsami.4c15832
ACS Appl. Mater. Interfaces 2025, 17, 7595–7606

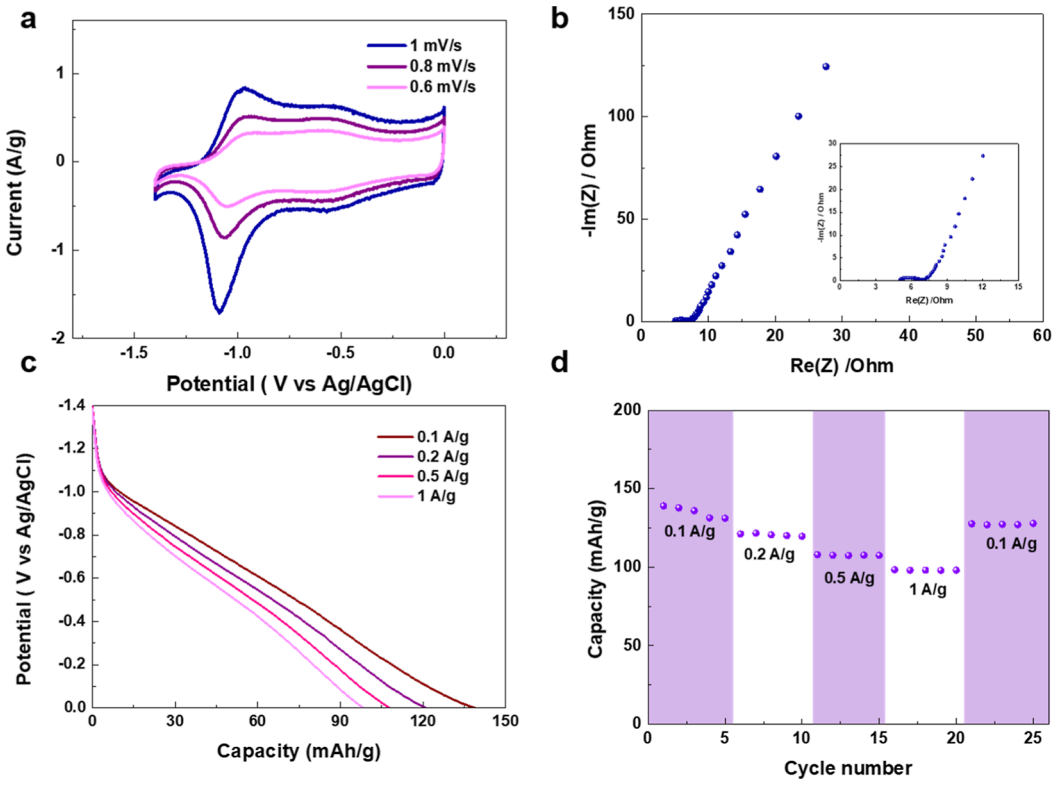

Figure 4. Electrochemical measurements of the VO_x-LSG anode in a three-electrode setup. (a) Cyclic voltammetry curves for VO_x-LSG at 0.6, 0.8, 1 mV s^{-1}. (b) Nyquist plots of VO_x-LSG with the high-frequency region in the inset. (c) Capacity-voltage profiles at 0.1, 0.2, 0.5, and 1 A g^{-1}. (d) Rate performance of VO_x-LSG cycled at different current densities.

(001), (110), and (211) planes. X-ray diffraction (XRD) analysis in Figure 2j shows three prominent peaks at 20.5°, 26.4°, and 36.0°, which are indexed to the (001), (110), and (211) planes of V_2O_5, respectively. This indicates that V_2O_5 is the predominant vanadium oxide species in the VO_x-LSG film. Additionally, the XRD pattern reveals minor peaks at 33.4° and 42.2°, corresponding to the $(10\bar{2})$ and (210) planes of VO_2, suggesting the presence of a small amount of VO_2 in the VO_x-LSG film.

XPS was performed to analyze the chemical composition of the VO_x-LSG film, with the deconvoluted V 2p spectra presented in Figure 2h. The spectrum reveals a peak at 516.6 eV corresponding to V^{4+}, and another at 517.8 eV associated with V^{5+}, indicating that the VO_x component in the VO_x-LSG composite comprises 74% V^{5+} and 26% V^{4+}. This mixed-valence state, with an effective chemical formula of $V_2O_{4.74}$, enhances electrical conductivity through electron hopping between V^{4+} and V^{5+}, and increases ionic conductivity by generating oxygen vacancies in the prepared material.[27,28] The O 1s spectra of the VO_x-LSG composite (Figure S2b) can be deconvoluted into three peaks at 531.3, 533.8, and 535.5 eV, corresponding to V−O−V, C═O, and C−O bonds, respectively, thereby confirming the presence of VO_x. Similarly, the C 1s peak for the VO_x-LSG composite is deconvoluted into peaks at 284.7, 285.7, 286.6, 288.0, and 289.1 eV, representing C═C, C−C, C−O, C═O, and COOH bonds, respectively, which verifies the reduction of graphene oxide (Figure S2a). The Raman spectrum (Figure 2i) illustrates the D and G peaks associated with graphene oxide. Peaks O1, O2, and O3 of the VO_x denote out-of-plane terminal, in-plane terminal, and in-plane bridging oxygen atoms in V_2O_5, respectively, with all peaks labeled according to their respective vibrational modes.[29]

To make a full cell, $Na_{1.88}Mn[Fe(CN)_6]_{0.97}$ (NaMnHCF) was selected as the cathode. The SEM images (Figure 3a,b) demonstrate the cubic structure. Energy dispersive spectroscopy (EDS) mapping shows that sodium (Na) (Figure 3c), manganese (Mn) (Figure 3d), and iron (Fe) (Figure 3e) are uniformly distributed throughout the NaMnHCF film. TEM images and SAED patterns were taken on NaMnHCF films. The TEM image clearly shows the cubic structure and the size of the cubes are around 100 nm (Figure 3f). The SAED pattern (Figure 3g) also reveals the $Na_{1.88}Mn[Fe(CN)_6]_{0.97}$ structure. The (200), (220) and (400) planes can be clearly seen in the SAED image. The 3 sharp peaks at 17.1°, 24.0°, and 34.4° in the XRD (Figure 3h) can be indexed to the (200), (220) and (400) of $Na_{1.88}Mn[Fe(CN)_6]_{0.97}$, respectively. This further confirms the successful synthesis of $Na_{1.88}Mn[Fe(CN)_6]_{0.97}$. The XRD peaks (Figure 3h) indicate that the NaMnHCF material is monoclinic with P21/n symmetry, consistent with that reported in the literature.[30]

The electrochemical performance of the VO_x-LSG anode were examined using a three-electrode configuration within a voltage range of 0 to −1.4 V vs Ag/AgCl, with 17.0 M $NaClO_4$ and 0.33 M $Na_4Fe(CN)_6$ used as the electrolyte. Figure 4a exhibits the cyclic voltammetry (CV) plot, which shows broad peaks with minimal peak-to-peak separation, characteristic of rapid Faradaic charge storage processes typical of redox-active pseudocapacitive materials. Figure 4b provides the Nyquist plot, which reveals a relatively low charge transfer resistance (R_{ct} = 2 Ω), suggesting that the VO_x-LSG film offers both high electronic and ionic conductivity. The voltage profile depicted in Figures 4c and S8a shows a sloping behavior within the −1.4 to 0 V range, signifying that the observed capacity primarily originates from surface-controlled processes. Figure 4d

https://doi.org/10.1021/acsami.4c15832
ACS Appl. Mater. Interfaces 2025, 17, 7595−7606

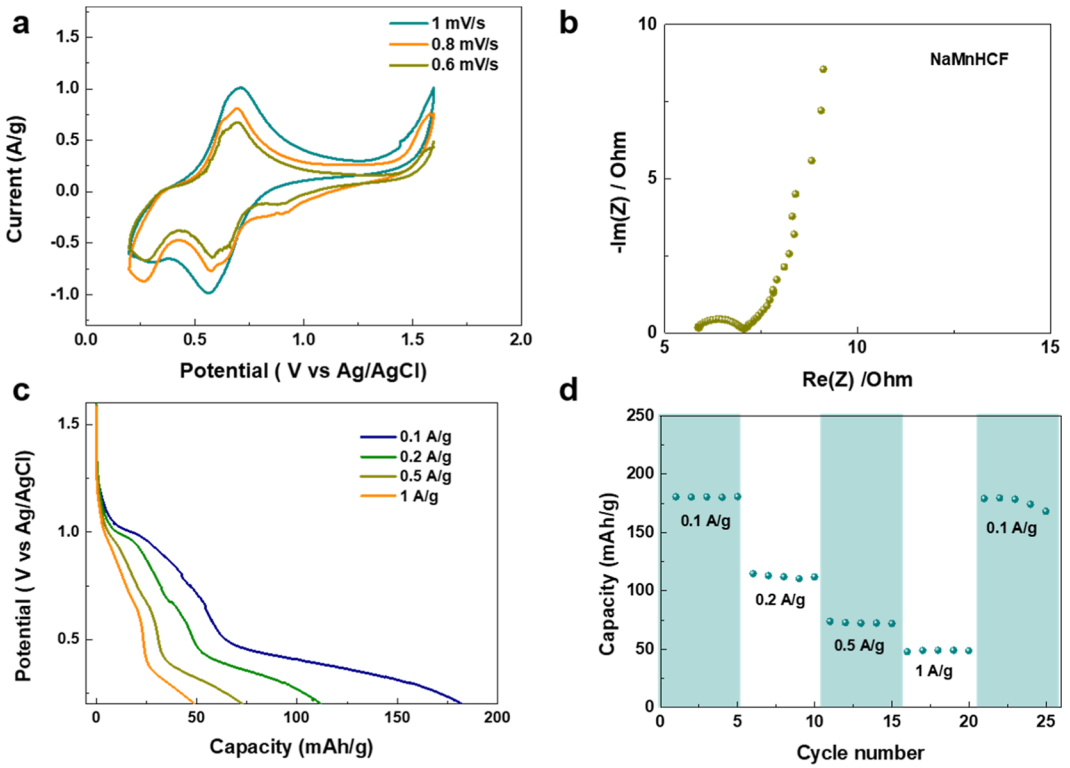

Figure 5. Electrochemical measurements of the NaMnHCF cathode in a three-electrode setup. (a) Cyclic voltammetry curves for NaMnHCF at 0.6, 0.8, 1 mV s^{-1}. (b) Nyquist plots of NaMnHCF. (c) Capacity-voltage profiles at 0.1, 0.2, 0.5, and 1 A g^{-1}. (d) Rate performance of NaMnHCF cycled at different current densities.

illustrates the rate performance of the VO_x-LSG film. When the current densities are 0.1, 0.2, 0.5, and 1 A/g, the average discharge capacities achieved are 139, 121, 107, and 98 mA h/g, respectively, relative to the total mass of the VO_x-LSG composite. With increasing current density from 0.1 to 1 A/g, about 70% of the capacity was maintained. Furthermore, even after a rapid rate change, the VO_x-LSG electrode retained a discharge capacity of 128 mA h/g, with 92% of this capacity recoverable. These results highlight the electrode's exceptional fast-charging performance and rate stability, suggesting its potential for use in fast-charging applications within full cells.

The specific capacity of VO_x within the VO_x-LSG composite is determined as follows

$$\text{Specific capacity per } VO_x = \frac{(\text{total capacity} - \text{LSG spec. capacity} \times \text{LSG mass})}{VO_x \text{ mass}} = \frac{139 - 11}{0.736} = 173.9 \text{ mA h/g} \quad (1)$$

The contribution of LSG is limited to approximately 12 mA h/g, as demonstrated by the three-electrode test presented in Figure S3.

The electrochemical characteristics of the NaMnHCF cathode were investigated using a three-electrode system with a voltage range from 0.2 to 1.6 V vs Ag/AgCl, and using 17.0 M $NaClO_4$ + 0.33 M $Na_4Fe(CN)_6$ as the electrolyte. As illustrated in Figure 5a, oxidation and reduction peaks are observed around 0.6−0.7 V, indicating a battery-type behavior. The voltage profile depicted in Figures 5c and S8b reveals two distinct sloping regions with markedly different gradients. With the voltage range from 0.4−1.1 V vs Ag/AgCl, a sloping plateau is observed, with its capacity contribution decreasing as the current density increases, suggesting a rate-dependent battery-type behavior. This observation aligns with cyclic voltammetry (CV) results, where the most significant redox peaks are noted in the same potential range. Figure 5b presents the Nyquist impedance of $Na_{1.88}Mn[Fe(CN)_6]_{0.97}$ in the electrolyte, showing a relatively low resistance (R_{ct} = 1 Ω), which implies that $Na_{1.88}Mn[Fe(CN)_6]_{0.97}$ exhibits high electronic and ionic conductivity in the 17.0 M $NaClO_4$ + 0.33 M $Na_4Fe(CN)_6$ solution. Figure 5d illustrates the rate performance, with average discharge capacities of 180, 112, 72, and 49 mA h/g at current densities of 0.1, 0.2, 0.5, and 1 A/g, respectively. Moreover, the NaMnHCF electrode demonstrates a capacity recovery of 98%, reflecting its excellent fast-charging capability and significant rate stability. The peaks at high voltages in Figure 5a,c,e are due to the electrolyte decomposition. We have performed the cyclic voltammetry of the 17.0 M $NaClO_4$ + 0.33 M $Na_4Fe(CN)_6$ electrolyte and 17.0 M $NaClO_4$ electrolyte (reference electrode: Ag/AgCl; working electrode: glassy carbon; counter electrode: graphite) (Figure S12). The small oxidation and reduction peaks at 1.6 and −0.5 V can be attributed to the oxidation and the reduction of the additive $Na_4Fe(CN)_6$ in the electrolyte as there is no oxidation and reduction peak for 17.0 M $NaClO_4$ only. The peaks observed at high voltage 1.9−2.6 V are due to the decomposition of the $NaClO_4$ electrolyte.

The VO_x-LSG film was utilized as the anode and coupled with the NaMnHCF cathode in a full cell configuration using the 17.0 M $NaClO_4$ + 0.33 M $Na_4Fe(CN)_6$ electrolyte to simulate a more practical application. The electrochemical performance and kinetics of the full cell were assembled with VO_x-LSG as the anode and NaMnHCF as the cathode. Figure

https://doi.org/10.1021/acsami.4c15832
ACS Appl. Mater. Interfaces 2025, 17, 7595−7606

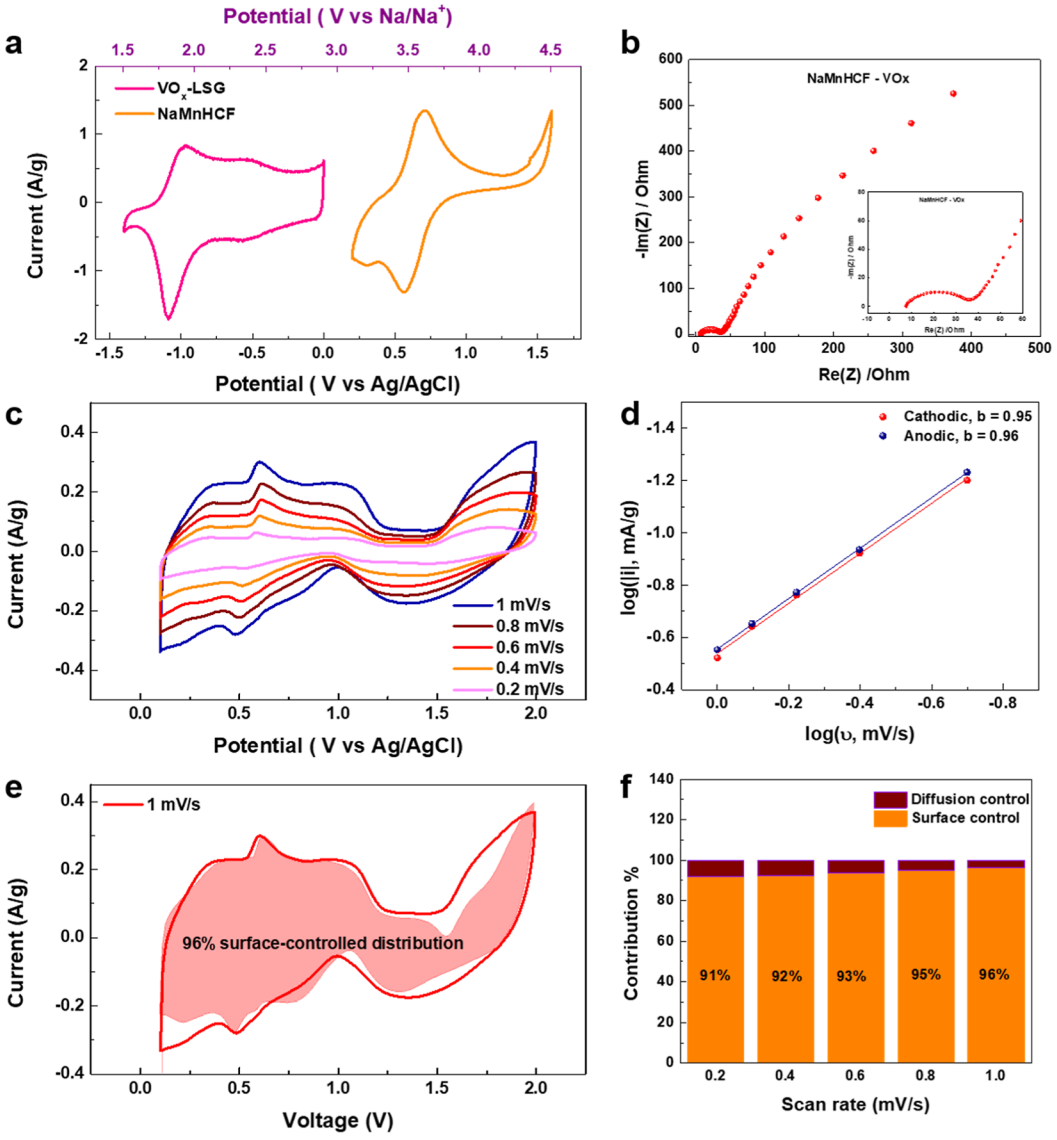

Figure 6. Electrochemical analysis of the NaMnHCF || VO_x-LSG cells. (a) Potential windows of VO_x-LSG and NaMnHCF in 17.0 M $NaClO_4$ + 0.33 M $Na_4Fe(CN)_6$ electrolyte. (b) Nyquist plots of NaMnHCF || VO_x-LSG full cell with the high-frequency region in the inset. (c) Cyclic voltammetry curves of a NaMnHCF || VO_x-LSG coin cell at 0.2, 0.4, 0.6, 0.8, and 1 mV/s. (d) *b*-values of the most pronounced pair of peaks in the CV. (e) Current contribution by surface-controlled processes at 1 mV/s. (f) Capacity contribution by surface-controlled and diffusion-controlled processes across a range of scan rates.

6a illustrates the cyclic voltammetry (CV) curves for the VO_x-LSG anode and NaMnHCF cathode in the 17.0 M $NaClO_4$ + 0.33 M $Na_4Fe(CN)_6$ electrolyte. The 17.0 M $NaClO_4$ + 0.33 M $Na_4Fe(CN)_6$ electrolyte provides an extended electrochemical window, with hydrogen and oxygen evolution potentials reaching −1.7 and 2.0 V, respectively (see Figure S4). This results in an electrochemical window of approximately 3.7 V, which supports the stable operation of both the VO_x-LSG anode and NaMnHCF cathode. The VO_x-LSG anode is electrochemically active within the voltage range from 1.51 to 2.91 V vs Na/Na^+, which encompasses the voltage ranges of typical aqueous sodium-ion battery anodes like $NaTi_2(PO4)_3$. The NaMnHCF cathode operates within the potential range of 3.11−4.51 V versus Na/Na^+, thereby offering a broader voltage window. Alternatively, when testing another cathode, $Na_{0.66}Mn_{0.66}Ti_{0.34}O_2$, in conjunction with the VO_x-LSG anode, it was observed that $Na_{0.66}Mn_{0.66}Ti_{0.34}O_2$ has a narrower potential range (3.11−3.91 V vs Na/Na^+) compared to NaMnHCF (Figure S5a). Consequently, the NaMnHCF cathode, with its higher potential, was favored for its wider voltage window and superior rate (Figure S5c) and cycling performance (Figure S5b). Figure 6b presents the Nyquist impedance for the NaMnHCF || VO_x-LSG coin cell within the electrolyte, showing a relatively low resistance (R_{ct} = 30 Ω). This indicates that the full cell exhibits high electronic and ionic conductivity in the 17.0 M $NaClO_4$ + 0.33 M $Na_4Fe(CN)_6$ electrolyte. Figure 6c illustrates the cyclic voltammetry (CV) data within a voltage range of 0.1−2 V. The pair of peaks observed between 0.3 and 0.8 V were examined in order to analyze the kinetics of the charge storage processes in the NaMnHCF || VO_x-LSG coin cell. The peak current (i) is attributed to two distinct contributions: battery-like diffusion-controlled processes and capacitor-like surface-controlled charge-storage processes. The peak current densities (i) and scan rates (v) relationship generally follows a power law[31]

https://doi.org/10.1021/acsami.4c15832
ACS Appl. Mater. Interfaces 2025, 17, 7595−7606

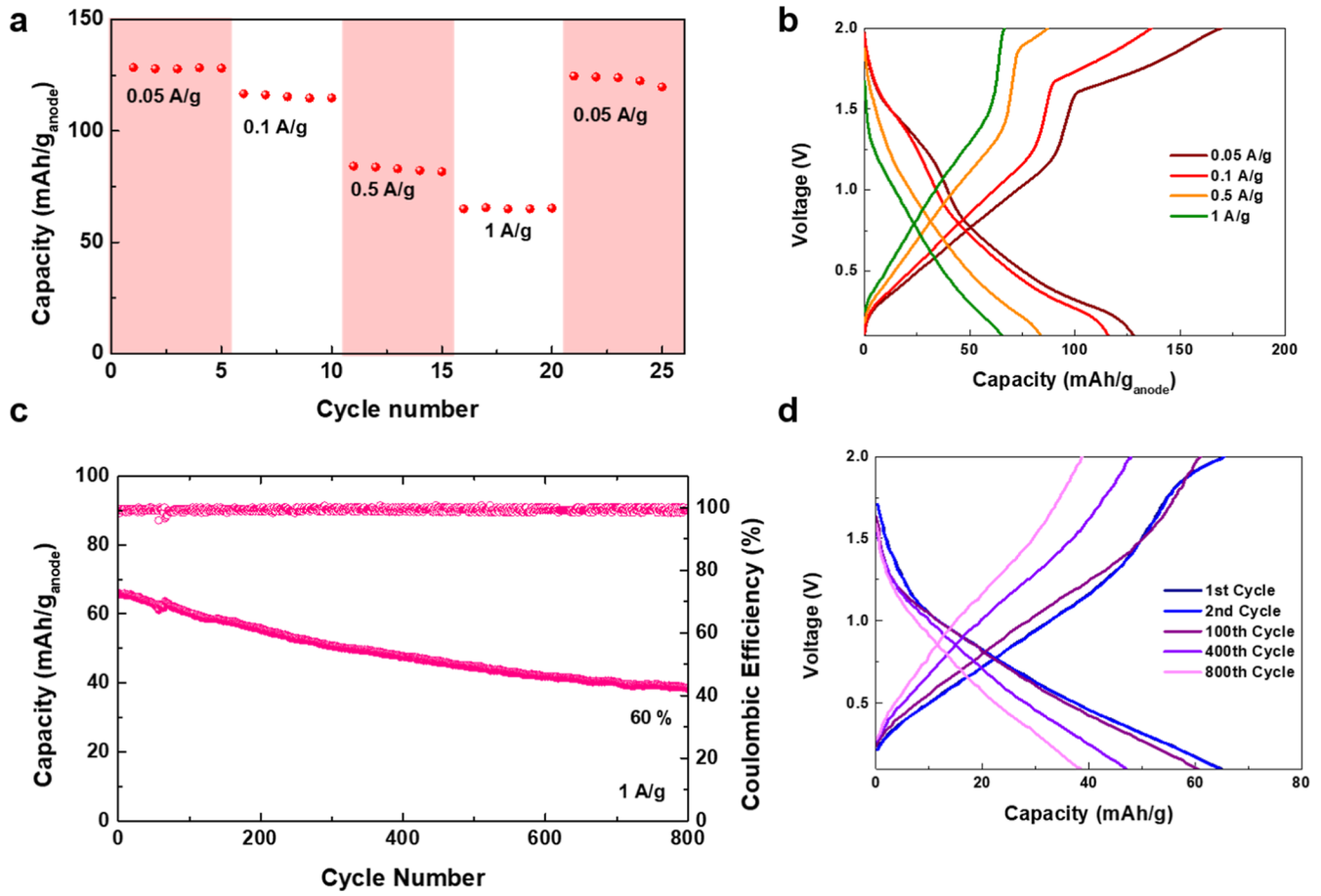

Figure 7. Electrochemical performance of the NaMnHCF || VO_x-LSG coin cells. (a) Rate performance of a NaMnHCF || VO_x-LSG cell cycled at 0.05, 0.1, 0.5 and 1 A/g. (b) Capacity-voltage profiles at different rates. (c) Capacity and Coulombic efficiency of a NaMnHCF || VO_x-LSG cell over 1 A/g cycling. (d) Capacity-voltage profiles of the 1st, 2nd, 100th, 400th, and 800th cycles during 1 A/g cycling.

$$i = av^b \tag{2}$$

For which a and b are constants determined experimentally. After plotting $\log(i)$ for each peak versus $\log(v)$, the value of b could be derived. A b value of 0.5 presents a diffusion-controlled charge-storage mechanism, whereas a b value of 1.0 signifies a surface-controlled capacitive charge-storage process.[29,32] Figure 6d shows that the anodic and cathodic peaks have b values of 0.96 and 0.95, respectively (R^2 = 0.995). These values indicate that the electrochemical reactions during charge and discharge are predominantly controlled by surface processes rather than diffusion throughout the entire operating potential range. Additionally, to further quantify the charge storage behavior and to separate the contributions from diffusion-controlled battery-type processes and surface-controlled capacitor-type processes, a secondary kinetic analysis was performed using the following relationship[33,34]

$$i = k_1 v + k_2 v^{1/2} \tag{3}$$

where k_1 and k_2 are the proportionality constants for the surface-controlled and diffusion-controlled contributions, respectively. Figure 6e illustrates an example in which the current contributions from these two processes were quantified using cyclic voltammetry (CV) data at a scan rate of 1 mV/s. As the scan rates increase, the proportion of surface-controlled charge storage rises from 91% at 0.2 mV/s to 96% at 1 mV/s (Figure 6f). The high b values and significant surface-controlled capacity contributions indicate that, even at very slow scan rates, the charge storage mechanism of the NaMnHCF || VO_x-LSG coin cell is predominantly directed by capacitive processes. This characteristic enhances both the fast-charging capability and the high-capacity performance of sodium-ion energy storage.

The electrochemical performance of the NaMnHCF || VO_x-LSG system was evaluated using 2016-type coin cells. The full cell demonstrates significantly improved rate performance. When the current densities are 0.05, 0.1, 0.5, and 1 A/g, the NaMnHCF || VO_x-LSG full cell attains high discharge capacities of 128, 116, 84, and 65 mA h/(g anode), or 64, 58, 42, and 33 mA h/g when calculated based on the total mass, respectively (Figure 7a). Figure 7b displays the rate capacities and charge−discharge profiles of the NaMnHCF || VO_x-LSG coin cell across the current densities from 0.05 to 1 A/g. The voltage profiles of NaMnHCF || VO_x-LSG coin cell display a minor plateau near 1.7 V and a voltage gradient in the 0.01−1.7 V range, signifying that the capacity is primarily governed by surface-controlled mechanisms. The observed plateau, characteristic of diffusion-controlled Faradaic processes, exhibits a steeper gradient at higher rates, indicating that the contribution of battery-type processes diminishes as the rate increases. This observation aligns with the kinetic analysis results shown in Figure 6f. Furthermore, even after a fast alteration in the rate, the NaMnHCF || VO_x-LSG coin cell maintains a discharge capacity of 124 mA h/g, with 97% of the

https://doi.org/10.1021/acsami.4c15832
ACS Appl. Mater. Interfaces 2025, 17, 7595−7606

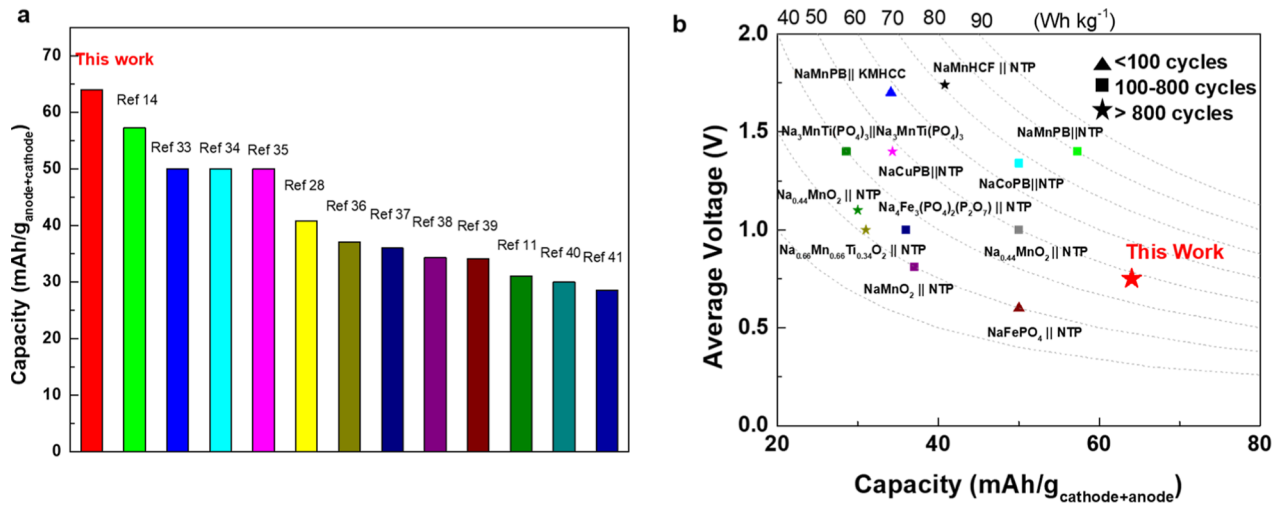

Figure 8. Performance comparison of NaMnHCF || VO_x-LSG to previously reported systems in the literature. (a) A capacity comparison based on total electrode mass of NaMnHCF || VO_x-LSG to those of other aqueous Na-ion batteries reported in the literature. (b) Comparison of the capacity, average voltage, specific energy, and cycling stability of this cell in work with those of other previously reported aqueous Na-ion batteries.

capacity being recoverable. This demonstrates the exceptional fast-charging performance and robust rate stability of the electrode.

At a high current density of 1 A/g, the NaMnHCF || VO_x-LSG coin cell achieved excellent long-term cycling stability (Figure 7c), retaining 80% of its capacity after 275 cycles and 60% after 800 cycles. Additionally, as depicted in Figure 7d, the charge and discharge curves during cycling at 1 A/g exhibit fewer distinct plateaus, primarily reflecting pseudocapacitive behavior. In addition, VO_x-LSG anodes can maintain their structural integrity during rapid and repeated insertion/extraction of Na^+ ions verifying from the XPS, SEM and TEM (Figures S9−11), respectively, before and after cycling. There are no significant structural or morphological changes observed. The stability in structure and morphology contributes to the good cycling performance of the VO_x-LSG anode.

Additionally, a set of control experiments were conducted to evaluate the effectiveness of 17.0 M $NaClO_4$ + 0.33 M $Na_4Fe(CN)_6$ water-in-salt electrolytes. These electrolytes are explored as a viable approach for stabilizing free-state water as well as extending the electrochemical stability window (ESW) of aqueous electrolytes.[17] To assess the ESW of various type of electrolytes, we investigated an 8.0 M $NaClO_4$ electrolyte and a 17.0 M $NaClO_4$ electrolyte, comparing these to the 17.0 M $NaClO_4$ + 0.33 M $Na_4Fe(CN)_6$ electrolyte. As illustrated in Figure S6a, the 17.0 M $NaClO_4$ electrolyte exhibits a potential window of −1.7 to 2.0 V. The modified 17.0 M $NaClO_4$ + 0.33 M $Na_4Fe(CN)_6$ electrolyte provides a comparable ESW of over 3.7 V, similar to the pure 17.0 M $NaClO_4$ electrolyte, suggesting that the inclusion of $Na_4Fe(CN)_6$ has a minimal effect on the ESW. Conversely, the 8.0 M $NaClO_4$ electrolyte has a narrower electrochemical window of 1.7 V (−0.4 to 1.3 V). The water-in-salt electrolyte, however, offers a significantly wider electrochemical window of approximately 3 V, ensuring stable operation for both the VO_x-LSG anode and the NaMnHCF cathode. The cycling performance of NaMnHCF || VO_x-LSG coin cells was evaluated using 8.0 M $NaClO_4$, 17.0 M $NaClO_4$, and 17.0 M $NaClO_4$ + 0.33 M $Na_4Fe(CN)_6$ electrolytes (Figure S6b). The 8.0 M $NaClO_4$ electrolyte demonstrated lower capacity and retention compared to the 17.0 M $NaClO_4$ + 0.33 M $Na_4Fe(CN)_6$ electrolyte, primarily due to its insufficient electrochemical window for the anode−cathode reactions. Similarly, the 17.0 M $NaClO_4$ electrolyte also exhibited reduced capacity and retention relative to the 17.0 M $NaClO_4$ + 0.33 M $Na_4Fe(CN)_6$ electrolyte. This is attributed to the fact that $Na_4Fe(CN)_6$ prevents the dissolution of manganese, which is known to occur during the charging process in aqueous sodium-ion batteries.[17] During the charging process in aqueous sodium-ion batteries, the Mn−N6 octahedra in MnPB change from stable Mn^{2+} to unstable Mn^{3+}, inducing Mn dissolution and Mn vacancy formation on the surface. Continuous Mn dissolution leads to structural deformation and fast capacity decay.[35] Thus, Mn dissolution could be mitigated and even prevented[17] if the dislocating Mn can be trapped and nucleated deposits can subsequently grow epitaxially on the substrate. Earlier we mentioned that a very low concentration of $Na_4Fe(CN)_6$ as a Mn^{2+} trapping agent in a 17.6 M $NaClO_4$ electrolyte was used. The $Fe(CN)_6^{4-}$ wraps around the surface of each $Na_{1.88}Mn[Fe(CN)_6]_{0.97}$ particle to capture dislocating Mn in situ, therefore maintaining the integrity of the structure. In addition, the dissolved $Na_4Fe(CN)_6$ in an aqueous electrolyte solution is also considered as a redox-active electrolyte. A redox-active electrolyte could transport Na^+ ions for the anodic and cathodic reactions. In addition, it could also supply electrochemically active ionic species for extra charge transfer reactions (Figure 1b).[36] Hence, the overall capacity will increase with the combination of the cathode capacity and the aqueous redox-active electrolyte capacity. This could be confirmed by the specific capacity of NaMnHCF in 17.0 M $NaClO_4$ and 17.0 M $NaClO_4$ + 0.33 M $Na_4Fe(CN)_6$ with 0.1 A/g (Figure S13). Figure S13 shows that NaMnHCF has a capacity of 180 mA h/g in 17.0 M $NaClO_4$ + 0.33 M $Na_4Fe(CN)_6$ with two plateaus. The first one around 1.0 V is the reduction of NaMnHCF and the second one around 0.4 V is the reduction of $Fe(CN)_6^{4-}$ in the electrolyte solution. However, the capacity of NaMnHCF in 17.0 M $NaClO_4$ is around 112 mA h/g and there is only one plateau around 0.8 V because of the reduction of NaMnHCF. There is no plateau around 0.4 V. Therefore, the capacity at ∼0.4 V comes mainly from the reduction of $Na_4Fe(CN)_6$ in

https://doi.org/10.1021/acsami.4c15832
ACS Appl. Mater. Interfaces 2025, 17, 7595−7606

the electrolyte solution as the redox potential of $Fe(CN)_6^{3-}$/$Fe(CN)_6^{4-}$ is 0.36 V.

Another water-in-salt electrolyte, consisting of 9.0 M NaOTF (sodium trifluoromethanesulfonate) and 22.0 M TEAOTF (tetraethylammonium trifluoromethanesulfonate), was evaluated for use in NaMnHCF || VO_x-LSG coin cells due to its broad electrochemical window of approximately 4 V (−2.3 to 1.7 V) (Figure S7a). Despite this wide window, the electrolyte demonstrated inferior performance in terms of capacity at various rates (Figure S7c) and cycling stability (Figure S7b), primarily due to manganese dissolution. Consequently, the 17.0 M $NaClO_4$ + 0.33 M $Na_4Fe(CN)_6$ electrolyte is favored for NaMnHCF || VO_x-LSG coin cells, as it effectively mitigates Mn dissolution and maintains both high chemical and electrochemical stability in an aqueous environment.

Finally, the electrochemical performance of the NaMnHCF || VO_x-LSG coin cell was evaluated against other aqueous sodium-ion batteries documented in the literature. Figure 8a provides a comparison of the full-cell specific capacity, calculated based on the combined mass of both anode and cathode materials.[12,15,30,37−45] The NaMnHCF || VO_x-LSG coin cell demonstrates the highest specific capacity of 64 mA h/g among various tested systems. Figure 8b provides a comparative summary of the average voltage, energy density, and longevity for this system compared with previous reported aqueous sodium-ion batteries. It is evident that the NaMnHCF || VO_x-LSG full cell achieves high energy density, with a value of 47.7 W h/kg, calculated based on the total mass of both anode and cathode materials. Additionally, this system provides an impressive long-term cycling performance, sustaining 800 cycles with minimal capacity loss, thus surpassing most previously reported aqueous sodium-ion batteries. Consequently, the NaMnHCF || VO_x-LSG system not only offers adjustable energy density, but also represents a great option for fast-charging, long-term and safe energy storage applications.

CONCLUSIONS

In conclusion, the development of the VO_x-LSG composite through a simple two-step process—combining laser scribing and heating—represents a significant advance in the construction of high-performance anodes for aqueous sodium-ion batteries. Beginning with a VCl_3/GO precursor solution, the method reduces graphene oxide (GO) into laser-scribed graphene while ensuring the uniform distribution of nanosized VO_x particles. These nanoparticles provide numerous active sites for charge storage, contributing to the high specific capacity and rapid electrochemical kinetics observed. When used alongside a NaMnHCF cathode, the resulting full cell displays predominantly surface-controlled charge storage, which leads to fast charging and high capacity. The full cell achieves a specific capacity of 128 mA h/g at 0.05 A/g and exhibits remarkable rate performance. Additionally, the full cell demonstrates long-term stability, which retains 62% of its capacity after 800 cycles at 1 A/g, with an energy density of 47.7 W h/kg. The combination of high capacity, fast charging capabilities, and operational safety positions the NaMnHCF || VO_x-LSG full cell as a promising solution for future energy storage applications.

EXPERIMENTAL SECTION

Preparation of VO_x-LSG Composite. The VO_x-LSG composite was prepared starting with the synthesis of graphite oxide (GO) through a modified Hummers' method. First, 80 mg of VCl_3 (Sigma-Aldrich) were dissolved in 4.2 mL of deionized water and subjected to ultrasonic treatment for 2 h. Concurrently, 20 mg of freeze-dried GO powder was dissolved in 5.8 mL water, followed by 2 min of tip sonication. The VCl_3 solution was then gradually introduced into the GO dispersion using a syringe pump over a period of 2 h. The mixture was drop-cast onto graphite paper at a volume density of 200 $\mu L/cm^2$ and allowed to dry overnight.

Subsequently, the dried film underwent laser scribing with a 40 W Full Spectrum Laser Muse 2D Vision Desktop CO_2 Laser Cutter, operating at 12% power. The electrodes were then punched out from the film using a 10 mm hole punch. The punched electrodes were put in a tube furnace, initially set to 60 °C for 1 h. The temperature was then increased to 300 °C at a rate of 2 °C/min, where it was maintained for an additional hour. Finally, the VO_x-LSG electrodes were weighed using a microbalance, with the electrode masses ranging from 1.0 to 1.1 mg.

Preparation of $Na_{1.88}Mn[Fe(CN)_6]_{0.97}$. The $Na_{1.88}Mn[Fe(CN)_6]_{0.97}$ cathode was synthesized using a straightforward precipitation technique. Initially, 0.9681 g of $Na_4Fe(CN)_6{\cdot}10H_2O$ was dissolved in 100 mL of saturated NaCl solution, while 2.06 mmol of $MnSO_4{\cdot}H_2O$ was dissolved in 80 mL of the same saturated NaCl solution. Those two solutions were then stirred and gradually combined at 60 °C. After allowing the mixture to react for 12 h, the precipitate was obtained by centrifugation and thoroughly rinsed with DI water. After drying it in ambient air at 80 °C for 12 h, the final product was collected.

For the fabrication of composite cathode electrodes, carbon black (Super P), the active material, and polyvinylidene fluoride (PVDF) were mixed in a weight ratio of 2:7:1 and then compressed into electrodes. The mass of these electrodes was measured with a microbalance, yielding a mass range of 1.0−1.1 mg.

Electrolyte Preparation. The blank electrolyte, consisting of 17.0 M $NaClO_4$, was prepared by dissolving 24.5 g of $NaClO_4$ in 10 mL of deionized water. To create the modified electrolyte, which contains 17.0 M $NaClO_4$ and 0.33 M $Na_4Fe(CN)_6$, 24.5 g of $NaClO_4$ and 1 g of $Na_4Fe(CN)_6$ were dissolved in 10 mL of DI water.

Materials Characterization. XRD were collected using a PANalytical X'Pert PRO powder X-ray diffractometer over a range of 5° to 80° with the scan rate of 0.05°/s, employing Cu Kα radiation (λ = 1.54 Å) on a SiO_2 crystal zero-background plate. To avoid interference from graphite paper, glass slides were used as the substrate, and the active materials were manually scraped off to enhance the diffraction peaks. Unassigned minor peaks in the spectra are attributed to SiO_2 impurities. SEM images were obtained using a JEOL JSM-6610 SEM with an operating voltage of 30 kV. TEM and SAED were performed using a T12 TEM (FEI Inc.). Raman spectroscopy was performed with a Renishaw inVia confocal Raman microscope, utilizing a 633 nm laser. XPS was conducted with a Kratos Axis Ultra DLD spectrometer, which includes a monochromatic Al Kα X-ray source. The electrode mass was measured with a Mettler Toledo MX5 microbalance with a sensitivity of 0.001 mg. Thermogravimetric analysis (TGA) was carried out with a Thermogravimetric Analyzer TGA 8000 (PerkinElmer), employing heating from 30 to 800 °C at a rate of 10 °C/min. The airflow rate was 30 mL/min.

Electrochemical Testing. Cyclic voltammetry (CV), electrochemical impedance spectroscopy (EIS), and galvanostatic charge−discharge (GCD) tests were conducted with a Biologic VMP3 electrochemical workstation (model VMP3b-10, USA Science Instrument). The electrolyte used was a solution of 17.0 M sodium perchlorate ($NaClO_4$) with 0.33 M sodium ferrocyanide ($Na_4Fe(CN)_6$) in water. Coin cell evaluations were performed using an MTI battery cycler.

Coin Cell Assembly. CR2032 coin cells were used for this research and each coin cell use 150 μL 17.0 M $NaClO_4$ + 0.33 M

https://doi.org/10.1021/acsami.4c15832
ACS Appl. Mater. Interfaces 2025, 17, 7595−7606

$Na_4Fe(CN)_6$ electrolyte. A glass fiber sheet (GA-55, ADVANTEC) was used as a separator.

■ ASSOCIATED CONTENT

Supporting Information

The Supporting Information is available free of charge at https://pubs.acs.org/doi/10.1021/acsami.4c15832.

TGA, SEM, and XPS of different samples and different control experiment of electrochemical performances are provided in the Supporting Information (PDF)

■ AUTHOR INFORMATION

Corresponding Author

Richard B. Kaner − *Department of Chemistry and Biochemistry and Department of Materials Science and Engineering, University of California, Los Angeles, Los Angeles, California 90095, United States; California NanoSystem Institute (CNSI), University of California, Los Angeles, Los Angeles, California 90095, United States;* orcid.org/0000-0003-0345-4924; Email: kaner@chem.ucla.edu

Authors

Zhiyin Yang − *Department of Chemistry and Biochemistry, University of California, Los Angeles, Los Angeles, California 90095, United States*

Ailun Huang − *Department of Chemistry and Biochemistry, University of California, Los Angeles, Los Angeles, California 90095, United States;* orcid.org/0000-0002-9457-646X

Cheng-Wei Lin − *Department of Chemistry and Biochemistry, University of California, Los Angeles, Los Angeles, California 90095, United States;* orcid.org/0000-0002-3358-7827

Bradley C. Kroes − *Department of Chemistry and Biochemistry, University of California, Los Angeles, Los Angeles, California 90095, United States*

Xueying Chang − *Department of Chemistry and Biochemistry, University of California, Los Angeles, Los Angeles, California 90095, United States*

Maher F. El-Kady − *Department of Chemistry and Biochemistry, University of California, Los Angeles, Los Angeles, California 90095, United States*

Yuzhang Li − *Department of Chemical and Biomolecular Engineering, University of California Los Angeles, Los Angeles, California 90095-1569, United States; California NanoSystem Institute (CNSI), University of California, Los Angeles, Los Angeles, California 90095, United States;* orcid.org/0000-0002-1502-7869

Complete contact information is available at: https://pubs.acs.org/10.1021/acsami.4c15832

Notes

The authors declare no competing financial interest.

■ ACKNOWLEDGMENTS

The authors would like to thank the University of California Climate Action Seed Grant R02CP7008 (Y.L. and R.B.K.) for financial support along with the Dr. Myung Ki Hong Endowed Chair in Materials Innovation at UCLA (R.B.K.).

■ REFERENCES

(1) Zhang, H.; Liu, X.; Li, H.; Hasa, I.; Passerini, S. Challenges and Strategies for High-Energy Aqueous Electrolyte Rechargeable Batteries. *Angew. Chem., Int. Ed.* **2021**, *60* (2), 598−616.

(2) Choi, J. W.; Aurbach, D. Promise and Reality of Post-Lithium-Ion Batteries with High Energy Densities. *Nat. Rev. Mater.* **2016**, *1* (4), 16013.

(3) Larcher, D.; Tarascon, J.-M. Towards Greener and More Sustainable Batteries for Electrical Energy Storage. *Nat. Chem.* **2015**, *7* (1), 19−29.

(4) Yabuuchi, N.; Kubota, K.; Dahbi, M.; Komaba, S. Research Development on Sodium-Ion Batteries. *Chem. Rev.* **2014**, *114* (23), 11636−11682.

(5) Katsuyama, Y.; Yang, Z.; Thiel, M.; Zhang, X.; Chang, X.; Lin, C.; Huang, A.; Wang, C.; Li, Y.; Kaner, R. B. A Rapid Scalable Laser-Scribing Process to Prepare Si/Graphene Composites for Lithium-Ion Batteries. *Small* **2024**, *20* (28), 2305921.

(6) Katsuyama, Y.; Li, Y.; Uemura, S.; Yang, Z.; Anderson, M.; Wang, C.; Lin, C.-W.; Li, Y.; Kaner, R. B. Reprecipitation: A Rapid Synthesis of Micro-Sized Silicon-Graphene Composites for Long-Lasting Lithium-Ion Batteries. *ACS Appl. Mater. Interfaces* **2024**, *16* (10), 12612−12623.

(7) Gong, Y.; Li, Y.; Li, Y.; Liu, M.; Feng, X.; Sun, Y.; Wu, F.; Wu, C.; Bai, Y. Unraveling the Intrinsic Origin of the Superior Sodium-Ion Storage Performance of Metal Selenides Anode in Ether-Based Electrolytes. *Nano Lett.* **2024**, *24* (27), 8427−8435.

(8) Kim, H.; Hong, J.; Park, K.-Y.; Kim, H.; Kim, S.-W.; Kang, K. Aqueous Rechargeable Li and Na Ion Batteries. *Chem. Rev.* **2014**, *114* (23), 11788−11827.

(9) Liu, B.; Huang, A.; Yuan, X.; Chang, X.; Yang, Z.; Lyle, K.; Kaner, R. B.; Li, Y. Laser-Scribed Battery Electrodes for Ultrafast Zinc-Ion Energy Storage. *Adv. Mater.* **2024**, *36*, 2404796.

(10) Huang, A.; Yang, Z.; Chang, X.; Lin, C.-W.; Kaner, R. B. A Nanoengineered Vanadium Oxide Composite as a High-Performance Anode for Aqueous Li-Ion Hybrid Batteries. *Nanoscale Horiz.* **2024**, *9* (8), 1279−1289.

(11) Wang, F.; Borodin, O.; Gao, T.; Fan, X.; Sun, W.; Han, F.; Faraone, A.; Dura, J. A.; Xu, K.; Wang, C. Highly Reversible Zinc Metal Anode for Aqueous Batteries. *Nat. Mater.* **2018**, *17* (6), 543−549.

(12) Suo, L.; Borodin, O.; Wang, Y.; Rong, X.; Sun, W.; Fan, X.; Xu, S.; Schroeder, M. A.; Cresce, A. V.; Wang, F.; Yang, C.; Hu, Y.; Xu, K.; Wang, C. Water-in-Salt" Electrolyte Makes Aqueous Sodium-Ion Battery Safe, Green, and Long-Lasting. *Adv. Energy Mater.* **2017**, *7* (21), 1701189.

(13) Leonard, D. P.; Wei, Z.; Chen, G.; Du, F.; Ji, X. Water-in-Salt Electrolyte for Potassium-Ion Batteries. *ACS Energy Lett.* **2018**, *3* (2), 373−374.

(14) Hasegawa, G.; Kanamori, K.; Kiyomura, T.; Kurata, H.; Abe, T.; Nakanishi, K. Hierarchically Porous Carbon Monoliths Comprising Ordered Mesoporous Nanorod Assemblies for High-Voltage Aqueous Supercapacitors. *Chem. Mater.* **2016**, *28* (11), 3944−3950.

(15) Hou, Z.; Zhang, X.; Chen, J.; Qian, Y.; Chen, L.; Lee, P. S. Towards High-Performance Aqueous Sodium Ion Batteries: Constructing Hollow $NaTi_2(PO_4)_3$@C Nanocube Anode with Zn Metal-Induced Pre-Sodiation and Deep Eutectic Electrolyte. *Adv. Energy Mater.* **2022**, *12* (14), 2104053.

(16) Wang, P.; You, Y.; Yin, Y.; Guo, Y. Layered Oxide Cathodes for Sodium-Ion Batteries: Phase Transition, Air Stability, and Performance. *Adv. Energy Mater.* **2018**, *8* (8), 1701912.

(17) Liang, Z.; Tian, F.; Yang, G.; Wang, C. Enabling Long-Cycling Aqueous Sodium-Ion Batteries via Mn Dissolution Inhibition Using Sodium Ferrocyanide Electrolyte Additive. *Nat. Commun.* **2023**, *14* (1), 3591.

(18) Zhang, Q.; Man, P.; He, B.; Li, C.; Li, Q.; Pan, Z.; Wang, Z.; Yang, J.; Wang, Z.; Zhou, Z.; Lu, X.; Niu, Z.; Yao, Y.; Wei, L. Binder-Free NaTi2(PO4)3 Anodes for High-Performance Coaxial-Fiber Aqueous Rechargeable Sodium-Ion Batteries. *Nano Energy* **2020**, *67*, 104212.

(19) Yue, J.; Li, S.; Chen, S.; Yang, J.; Lu, X.; Li, Y.; Zhao, R.; Wu, C.; Bai, Y. Initiating High-Voltage Multielectron Reactions in NASICON Cathodes for Aqueous Zinc/Sodium Batteries. *Energy Mater. Adv.* **2023**, *4*, 0050.
(20) Jia, X.; Tian, R.; Liu, C.; Zheng, J.; Tian, M.; Cao, G. Stability and Kinetics Enhancement of Hydrated Vanadium Oxide via Sodium-Ion Pre-Intercalation. *Mater. Today Energy* **2022**, *28*, 101063.
(21) Wei, Q.; DeBlock, R. H.; Butts, D. M.; Choi, C.; Dunn, B. Pseudocapacitive Vanadium-based Materials toward High-Rate Sodium-Ion Storage. *Energy Environ. Mater.* **2020**, *3* (3), 221−234.
(22) Huang, A.; El-Kady, M. F.; Chang, X.; Anderson, M.; Lin, C.; Turner, C. L.; Kaner, R. B. Facile Fabrication of Multivalent VO_x/Graphene Nanocomposite Electrodes for High-Energy-Density Symmetric Supercapacitors. *Adv. Energy Mater.* **2021**, *11* (26), 2100768.
(23) Wang, L. J.; El-Kady, M. F.; Dubin, S.; Hwang, J. Y.; Shao, Y.; Marsh, K.; McVerry, B.; Kowal, M. D.; Mousavi, M. F.; Kaner, R. B. Flash Converted Graphene for Ultra-High Power Supercapacitors. *Adv. Energy Mater.* **2015**, *5* (18), 1500786.
(24) Hwang, J. Y.; El-Kady, M. F.; Wang, Y.; Wang, L.; Shao, Y.; Marsh, K.; Ko, J. M.; Kaner, R. B. Direct Preparation and Processing of Graphene/RuO 2 Nanocomposite Electrodes for High-Performance Capacitive Energy Storage. *Nano Energy* **2015**, *18*, 57−70.
(25) Hwang, J. Y.; El-Kady, M. F.; Li, M.; Lin, C.-W.; Kowal, M.; Han, X.; Kaner, R. B. Boosting the Capacitance and Voltage of Aqueous Supercapacitors via Redox Charge Contribution from Both Electrode and Electrolyte. *Nano Today* **2017**, *15*, 15−25.
(26) Hu, P.; Hu, P.; Vu, T. D.; Li, M.; Wang, S.; Ke, Y.; Zeng, X.; Mai, L.; Long, Y. Vanadium Oxide: Phase Diagrams, Structures, Synthesis, and Applications. *Chem. Rev.* **2023**, *123* (8), 4353−4415.
(27) Pang, Q.; Sun, C.; Yu, Y.; Zhao, K.; Zhang, Z.; Voyles, P. M.; Chen, G.; Wei, Y.; Wang, X. $H_2V_3O_8$ Nanowire/Graphene Electrodes for Aqueous Rechargeable Zinc Ion Batteries with High Rate Capability and Large Capacity. *Adv. Energy Mater.* **2018**, *8* (19), 1800144.
(28) Zhao, J.; Ren, H.; Liang, Q.; Yuan, D.; Xi, S.; Wu, C.; Manalastas, W.; Ma, J.; Fang, W.; Zheng, Y.; Du, C.-F.; Srinivasan, M.; Yan, Q. High-Performance Flexible Quasi-Solid-State Zinc-Ion Batteries with Layer-Expanded Vanadium Oxide Cathode and Zinc/Stainless Steel Mesh Composite Anode. *Nano Energy* **2019**, *62*, 94−102.
(29) Smirnov, M. B.; Roginskii, E. M.; Smirnov, K. S.; Baddour-Hadjean, R.; Pereira-Ramos, J.-P. Unraveling the Structure−Raman Spectra Relationships in V_2O_5 Polymorphs via a Comprehensive Experimental and DFT Study. *Inorg. Chem.* **2018**, *57* (15), 9190−9204.
(30) Jiang, L.; Liu, L.; Yue, J.; Zhang, Q.; Zhou, A.; Borodin, O.; Suo, L.; Li, H.; Chen, L.; Xu, K.; Hu, Y. High-Voltage Aqueous Na-Ion Battery Enabled by Inert-Cation-Assisted Water-in-Salt Electrolyte. *Adv. Mater.* **2020**, *32* (2), 1904427.
(31) Augustyn, V.; Come, J.; Lowe, M. A.; Kim, J. W.; Taberna, P.-L.; Tolbert, S. H.; Abruña, H. D.; Simon, P.; Dunn, B. High-Rate Electrochemical Energy Storage through Li+ Intercalation Pseudocapacitance. *Nat. Mater.* **2013**, *12* (6), 518−522.
(32) Sun, D.; Tang, Y.; He, K.; Ren, Y.; Liu, S.; Wang, H. Long-Lived Aqueous Rechargeable Lithium Batteries Using Mesoporous LiTi2(PO4)3@C Anode. *Sci. Rep.* **2015**, *5* (1), 17452.
(33) Liu, T.-C.; Pell, W. G.; Conway, B. E.; Roberson, S. L. Behavior of Molybdenum Nitrides as Materials for Electrochemical Capacitors: Comparison with Ruthenium Oxide. *J. Electrochem. Soc.* **1998**, *145* (6), 1882−1888.
(34) Wang, J.; Polleux, J.; Lim, J.; Dunn, B. Pseudocapacitive Contributions to Electrochemical Energy Storage in TiO_2 (Anatase) Nanoparticles. *J. Phys. Chem. C* **2007**, *111* (40), 14925−14931.
(35) He, R.; Lei, S.; Liu, M.; Qin, M.; Zhong, W.; Cheng, S.; Xie, J. Enhanced Dynamic Phase Stability and Suppressed Mn Dissolution in Low-Tortuosity Spinel LMO Electrode. *Energy Mater. Adv.* **2022**, *2022*, 0003.
(36) Senthilkumar, S. T.; Bae, H.; Han, J.; Kim, Y. Enhancing Capacity Performance by Utilizing the Redox Chemistry of the Electrolyte in a Dual-Electrolyte Sodium-Ion Battery. *Angew. Chem.* **2018**, *130* (19), 5433−5437.
(37) Liu, T.; Wu, H.; Du, X.; Wang, J.; Chen, Z.; Wang, H.; Sun, J.; Zhang, J.; Niu, J.; Yao, L.; Zhao, J.; Cui, G. Water-Locked Eutectic Electrolyte Enables Long-Cycling Aqueous Sodium-Ion Batteries. *ACS Appl. Mater. Interfaces* **2022**, *14* (29), 33041−33051.
(38) Wu, X.; Sun, M.; Guo, S.; Qian, J.; Liu, Y.; Cao, Y.; Ai, X.; Yang, H. Vacancy-Free Prussian Blue Nanocrystals with High Capacity and Superior Cyclability for Aqueous Sodium-Ion Batteries. *ChemNanoMat* **2015**, *1* (3), 188−193.
(39) Fernández-Ropero, A. J.; Saurel, D.; Acebedo, B.; Rojo, T.; Casas-Cabanas, M. Electrochemical Characterization of NaFePO4 as Positive Electrode in Aqueous Sodium-Ion Batteries. *J. Power Sources* **2015**, *291*, 40−45.
(40) Hou, Z.; Li, X.; Liang, J.; Zhu, Y.; Qian, Y. An Aqueous Rechargeable Sodium Ion Battery Based on a $NaMnO_2$ − $NaTi_2(PO_4)_3$ Hybrid System for Stationary Energy Storage. *J. Mater. Chem. A* **2015**, *3* (4), 1400−1404.
(41) Lee, M. H.; Kim, S. J.; Chang, D.; Kim, J.; Moon, S.; Oh, K.; Park, K.-Y.; Seong, W. M.; Park, H.; Kwon, G.; Lee, B.; Kang, K. Toward a Low-Cost High-Voltage Sodium Aqueous Rechargeable Battery. *Mater. Today* **2019**, *29*, 26−36.
(42) Wu, X.; Sun, M.; Shen, Y.; Qian, J.; Cao, Y.; Ai, X.; Yang, H. Energetic Aqueous Rechargeable Sodium-Ion Battery Based on $Na_2CuFe(CN)_6$ − $NaTi_2(PO_4)_3$ Intercalation Chemistry. *ChemSusChem* **2014**, *7* (2), 407−411.
(43) Nakamoto, K.; Sakamoto, R.; Sawada, Y.; Ito, M.; Okada, S. Over 2 V Aqueous Sodium-Ion Battery with Prussian Blue-Type Electrodes. *Small Methods* **2019**, *3* (4), 1800220.
(44) Li, Z.; Young, D.; Xiang, K.; Carter, W. C.; Chiang, Y. Towards High Power High Energy Aqueous Sodium-Ion Batteries: The $NaTi_2(PO_4)_3$/$Na_{0.44}MnO_2$ System. *Adv. Energy Mater.* **2013**, *3* (3), 290−294.
(45) Gao, H.; Goodenough, J. B. An Aqueous Symmetric Sodium-Ion Battery with NASICON-Structured $Na_3MnTi(PO_4)_3$. *Angew. Chem.* **2016**, *128* (41), 12960−12964.

https://doi.org/10.1021/acsami.4c15832
ACS Appl. Mater. Interfaces 2025, 17, 7595−7606